

## Real-time characterization of dislocation slip and twinning of shock-compressed molybdenum single crystals

Vatsa Gandhi <sup>1,\*</sup>, Suraj Ravindran <sup>2</sup>, Akshay Joshi <sup>3</sup>, and Guruswami Ravichandran <sup>1,4</sup>

<sup>1</sup>*Division of Engineering and Applied Science, California Institute of Technology, Pasadena, California 91125, USA*

<sup>2</sup>*Department of Aerospace Engineering and Mechanics, University of Minnesota, Minneapolis, Minnesota 55455, USA*

<sup>3</sup>*Engineering Department, Cambridge University, Cambridge CB2 1PZ, United Kingdom*

<sup>4</sup>*Jio Institute, Ulwe, Navi Mumbai, Maharashtra 410206, India*



(Received 24 January 2023; revised 12 May 2023; accepted 12 June 2023; published 6 July 2023)

Characterizing the fundamental micromechanisms activated during plastic deformation is critical to explain the macroscopic shock response of materials and develop accurate material models. In this paper, we investigate the orientation dependence, and the mediated slip and twin systems on [1 0 0] and [1 1 1] bcc molybdenum single crystals shock compressed up to 18 GPa with real-time Laue x-ray diffraction measurements. We report that dislocation slip along the {1 1 0}⟨1 1 1⟩ and {1 1 2}⟨1 1 1⟩ systems is the governing deformation mechanism during compression with negligible anisotropy observed at the Hugoniot state. We provide real-time evidence that molybdenum undergoes deformation twinning along {1 1  $\bar{2}$ }⟨1 1 1⟩ during shock release.

DOI: [10.1103/PhysRevMaterials.7.073601](https://doi.org/10.1103/PhysRevMaterials.7.073601)

### I. INTRODUCTION

When a metal undergoes shock compression beyond its Hugoniot elastic limit (HEL), the plastic deformation is typically governed by generation and motion of dislocations [1]. Generally, establishing the active atomistic mechanisms during inelastic loading is difficult but is critical to explain the macroscopic response of materials for shock applications involving high-velocity impacts such as planetary impacts [2], aircraft collisions [3], spacecraft shielding [4], and even armor and antiarmor applications [5]. The high strain rates, temperatures, and pressures experienced under shock compression may activate different slip or twin systems than under quasistatic loading and thus require real-time characterization of the atomistics. However, most studies to date focus on postmortem analysis of recovered samples which may not reflect the material behavior during the passage of the shock wave. To that end, recent efforts at the Dynamic Compression Sector (DCS) at the Advanced Photon Source (APS) [6] have enabled real-time x-ray diffraction (XRD) measurements in shock compression experiments and have been critical in understanding phenomena such as phase transformations [7,8] and equations of state [9–11].

Because of its high-temperature specific strength, creep resistance, and ductility [12], body-centered cubic (bcc) refractory metals, such as molybdenum (Mo), and their alloys have significant technological implications motivating studying their high-strain-rate material response. Plasticity in bcc metals is governed by dislocation slip along the [1 1 1] direction [13] and is mediated by various factors such as interactions of defects with grain boundaries, the influence of preexisting defects, and crystal structure [14]. Here, we focus

on molybdenum single crystals as a representative refractory bcc metal since single crystals help preclude the effect of grain boundaries on the deformation response and provide key insights concerning the role of crystal orientation.

Considerable work has been conducted to understand the fundamental deformation mechanisms of molybdenum in the quasistatic regime and it has been shown that its deformation is governed by the mobility of screw dislocations along the {1 1 0}⟨1 1 1⟩ and {1 1 2}⟨1 1 1⟩ slip systems. At low temperatures, the deformation of molybdenum is governed by thermally activated kink pairs and kink pair migration of screw dislocations along {1 1 0} slip planes [15–17] while at higher temperatures, the deformation is governed by cross slip along {1 1 2} planes [15]. Molybdenum also displays slip and yield tension-compression asymmetry due to the different Peirels stress in the twinning and antitwining [16,18–21] direction, where the twinning is more prevalent at lower temperatures [18,22]. In addition to slip, deformation twinning in the {1 1 2} planes along the ⟨1 1 1⟩ direction [23,24] has been observed from postmortem analysis of molybdenum undergoing shock compression (high strain rate) or low-temperature deformation. It was shown that the volume fraction of twinning increases with pressure [24] while homogeneous distribution of initial dislocations from pre-straining prior to shock compression suppressed twin formation [23]. Regardless, further experiments are required to understand these deformation mechanisms.

Polycrystalline Mo has been studied over a wide range of high pressures (up to 1 TPa) using diamond anvil cell (DAC) [25], plate impact [26,27], and laser ramp compression [28] experiments. However, limited plate impact experimental studies have been performed on Mo single crystals [29–33]. Studies by Mandal *et al.* [30,31] at low normal stresses (12.5 GPa) and Oniyama *et al.* [32] at higher pressures (up to 110 GPa) both report strong orientation dependence

\*vgandhi@caltech.edu

TABLE I. Material properties of single-crystal molybdenum [32].

Orientation	$\rho$ (kg/m <sup>3</sup> )	$C_L$ (m/s)	$C_s$ (m/s)	$a_0$ (Å)	$V_c$ (Å <sup>3</sup> )
[1 0 0]	10220 ± 60	6836 ± 44	3300 ± 14	3.147	31.1616
[1 1 0]		6432 ± 3	3264 ± 4		
[1 1 1]		6319 ± 8	3666 ± 5		

on the Hugoniot elastic limit (HEL) [30–32]. The [1 1 1] orientation was shown to exhibit the highest elastic amplitude which increases proportionally to the impact stress [32] while the behaviors along [1 0 0] and [1 1 0] were comparable. Additionally, the authors observed attenuation of the elastic precursor as a function of time and propagation distance hypothesizing a change in active slip systems during this transition [31]. To explore the fundamental mechanisms governing this observed anisotropy, Mandal *et al.* [30,31] performed complementary crystal plasticity simulations but suggested that *in situ* experiments be performed.

In this paper, we explore the underlying microstructural reasons for the anisotropy of HEL, and the governing plastic deformation mechanisms at the Hugoniot (steady) shock state and during release using plate impact experiments coupled with dynamic *in situ* x-ray diffraction (XRD). The experimental observations are quantified using complimentary XRD simulations for extracting the lattice strains and stresses using which the active slip and twin deformation mechanisms are characterized.

## II. MATERIALS AND METHODS

Plate impact experiments were conducted on high-purity (99.99%) molybdenum single crystals oriented along the [1 0 0] and [1 1 1] directions at DCS. The ambient properties of the single crystals are displayed in Table I. The material was procured from Accumet Materials Co. (Ossining, New York) as a 20 mm diameter cylindrical stock and powder diffraction was conducted at Caltech to quantify the misalignment of the crystallographic orientation. If the misalignment exceeded 2°, the stock was cut into cylindrical disks at an angle to correct the misorientation. The Mo stock was cut to disks after which they were lapped flat on both sides and polished on one surface for *in situ* XRD measurements. Because the samples underwent this additional processing, powder diffraction was once again conducted on the [1 0 0] and [1 1 1] crystals which confirmed that the samples remained as an ideal single crystal. The diffraction data are presented in the Supplemental Material (SM) [34].

A front surface impact configuration with reflection geometry XRD was implemented for the plate impact experiments at DCS [Fig. 1(a)]. Here, a 2.5–4 mm thick molybdenum single crystal is impacted onto a ~1.5 mm polycarbonate window target at velocities ranging from 1800–2800 m/s corresponding to elastic normal stresses of 8–19 GPa. The polycarbonate window limits the achievable stresses in the experiment to below 22 GPa due to the x-ray transparency issues at higher pressures. Regardless, this configuration was implemented rather than using the molybdenum as a target with a window attached to its rear because the high impedance of molybdenum requires a high impedance window such as

c-cut sapphire. In addition, the thickness of the sapphire window required to hold the pressure would result in x-rays being fully absorbed at the experimental incidence angle. The experiments were conducted using the powder and two-stage light gas guns in Sector 35-Hutch E of the DCS using the 24-bunch mode with 153.4 ns x-ray interspacing and ~100 ps exposure time [6]. The white x-ray beam was generated using an

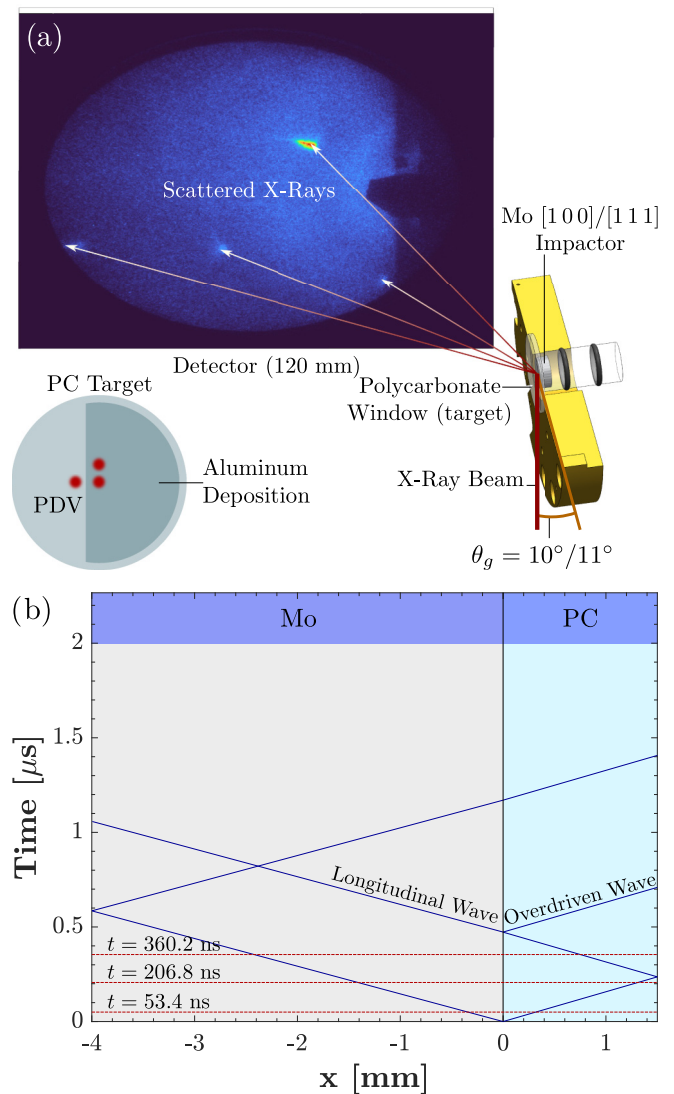


FIG. 1. (a) Schematic of the front surface plate impact and reflection geometry XRD configuration and (b) distance-time ( $x-t$ ) diagram indicating the designed XRD frame capture times. Here, time  $t = 0$  corresponds to the impact time and the first XRD frame, not illustrated, is designed to be obtained prior to impact at  $t = -100$  ns.

undulator with a 17.2 mm period (24 keV, 1st harmonic) and focused to a beam size of  $100 \times 800 \mu\text{m}$ . The reflection geometry was conducted at an x-ray-to-gun angle of  $\theta_g = 10\text{--}11$  degrees using a four-camera detector array with 120 mm fiber taper. These four charge-coupled device (CCD) cameras were perfectly synchronized with the synchrotron x-ray bunches using a delay generator and each camera was gated to capture one frame during the experiment [6,35]. A polychromatic x-ray spectrum is necessary since the dynamic experiments were conducted at a constant inclination angle ( $\theta_g$ ); thus, to obtain diffraction spots for varying  $d$  spacings, the wavelength must vary according to Bragg's law. The spectral scans of the x-rays of the 24-bunch mode for the different APS cycles are displayed in the SM.

The polycarbonate targets are attached to an aluminum target holder which houses a target optical beam block (TOBB) system. Here, a laser is illuminated from one end of the target holder using a fiber optic probe and is captured by a receiver probe on the other end. Due to the impact event and the x-ray event being completely independent, the events must be synchronized to ensure the proper frames are captured during an experiment. Given a desired projectile velocity, desired first-frame time with respect to impact, and known distance between the TOBB laser and impact surface, the necessary delays are calculated and applied to synchronize first-frame capture. Once the projectile crosses the TOBB laser, a series of oscilloscopes and delay generators are triggered and initiate diagnostics. Note that perfect synchronization between the impact event and APS electron bunch structure is impossible; thus, the actual first-frame capture can vary up to 153.4 ns. This means if the desired first frame is  $-100$  ns prior to impact, even with the exact desired impact velocity, the first-frame capture will occur between  $t = -100$  and 53.4 ns. As a result, any fluctuation from the desired impact velocity can affect the frame capture sequence [36].

As stated earlier, four XRD frames were obtained in each experiment spaced 153.4 ns apart. The front surface impact experiments were designed such that the first frame was obtained before impact ( $t = -100$  ns) to calibrate the Laue diffraction spots due to potential rotation of the projectile as it traverses the barrel. The last three frames are obtained at the Hugoniot state to understand the time-dependent response of the material from the movement of diffraction spots. At the pressures of interest (8–19 GPa), an overdriven wave traverses the polycarbonate sample and thus, with the current design for frame capture times, for the higher velocity experiments, only frames 2 and 3 capture the Hugoniot state. The 4th frame captures the release behavior of the molybdenum which provides important information on the elastic unloading behavior of the crystals. Additionally, due to uncertainties in gun powder explosion, the actual impact velocities deviated slightly from the desired values and thus, in some experiments, the first frame was captured immediately after impact resulting in the 4th frame capturing the release behavior even for lower pressure experiments. This late impact complicates the analysis of the diffraction spots and introduces uncertainties in the lattice strain calculations. The experimental design is illustrated in the time-distance ( $x$ - $t$ ) diagram in Fig. 1(b). Here, time  $t = 0$  corresponds to the impact time and the first XRD frame, not illustrated, is designed to be obtained at  $t = -100$  ns. Evolution

of the Laue spots from the XRD measurements were analyzed by simulating the experimental conditions in MATLAB [37] to extract the lattice strains and stresses for both single-crystal orientations. This requires knowledge of the detector distances which were obtained using a polycrystalline silicon standard prior to every shot and the diffraction pattern was analyzed using a combination of Dioptas software [38] and in-house polycrystalline XRD simulations. The full details of the silicon calibration is described in the SM.

In addition to the x-rays, macroscopic laser interferometry measurements, using photonic Doppler velocimetry (PDV) [39], were conducted simultaneously to link the microscopic and continuum response of the single crystals. Because the polycarbonate is transparent, an aluminum mirror, in the shape of a semicircle, was vapor deposited (150 nm thickness) onto the impact surface of the window as shown in Fig. 1(a) and in-material measurements were conducted through the polycarbonate. A total of three PDV probes were utilized in each experiment where one probe was placed in the transparent region looking down the barrel to measure the impact velocity while the other two probes were placed on the deposited region. Here, one probe was placed at the center of the sample to measure the in-material particle velocity and the other probe was slightly offset from the center. The representative velocity profiles are illustrated in Figs. 2(i) and 2(j). The velocity profiles of all experiments are plotted in the Supplemental Material.

### III. SIMULATION

As stated earlier, four XRD frames were captured during each experiment which contain information on the atomistic deformation of Mo single crystals. The representative diffraction spots for molybdenum shocked at  $\sim 10$  GPa and  $\sim 20$  GPa are shown in Fig. 2. During the shocked state, since the material undergoes compression, the crystallographic  $d$  spacing tends to decrease resulting in the spots shifting to higher azimuthal angles based on Bragg's law. This is illustrated in the diffraction data in Fig. 2(b). The radial and azimuthal shifts of the Laue spots contain information on the elastic lattice strains and rotations in the material. However, to quantify the atomistic deformation, the diffraction spots must first be indexed. This is done using Laue simulations in MATLAB [37].

Prior to indexing the spots, the x-ray and detector geometry were determined using silicon calibration discussed earlier. This provides information on the detector distance from the sample, the location on the detector at which the x-ray beam is incident, and the detector center. Using these parameters, the x-ray wavelength spectrum, and the known orientation of the sample (another axis beyond the sample normal) from powder diffraction conducted during sample preparation, the allowable x-ray diffracted wave vectors  $\mathbf{k}$  are determined using the methodology outlined in Sec. III of the SM. These vectors are projected onto a simulated detector screen and compared to the experimental diffraction spots. Note that the direction of the alternate axis is marked on the sample and the projectile is placed in the barrel along this orientation. However, since the projectile is allowed to rotate as it traverses the barrel, the actual crystal orientation is unknown during the experiment. Thus, if the simulation and experimental spots do not match,

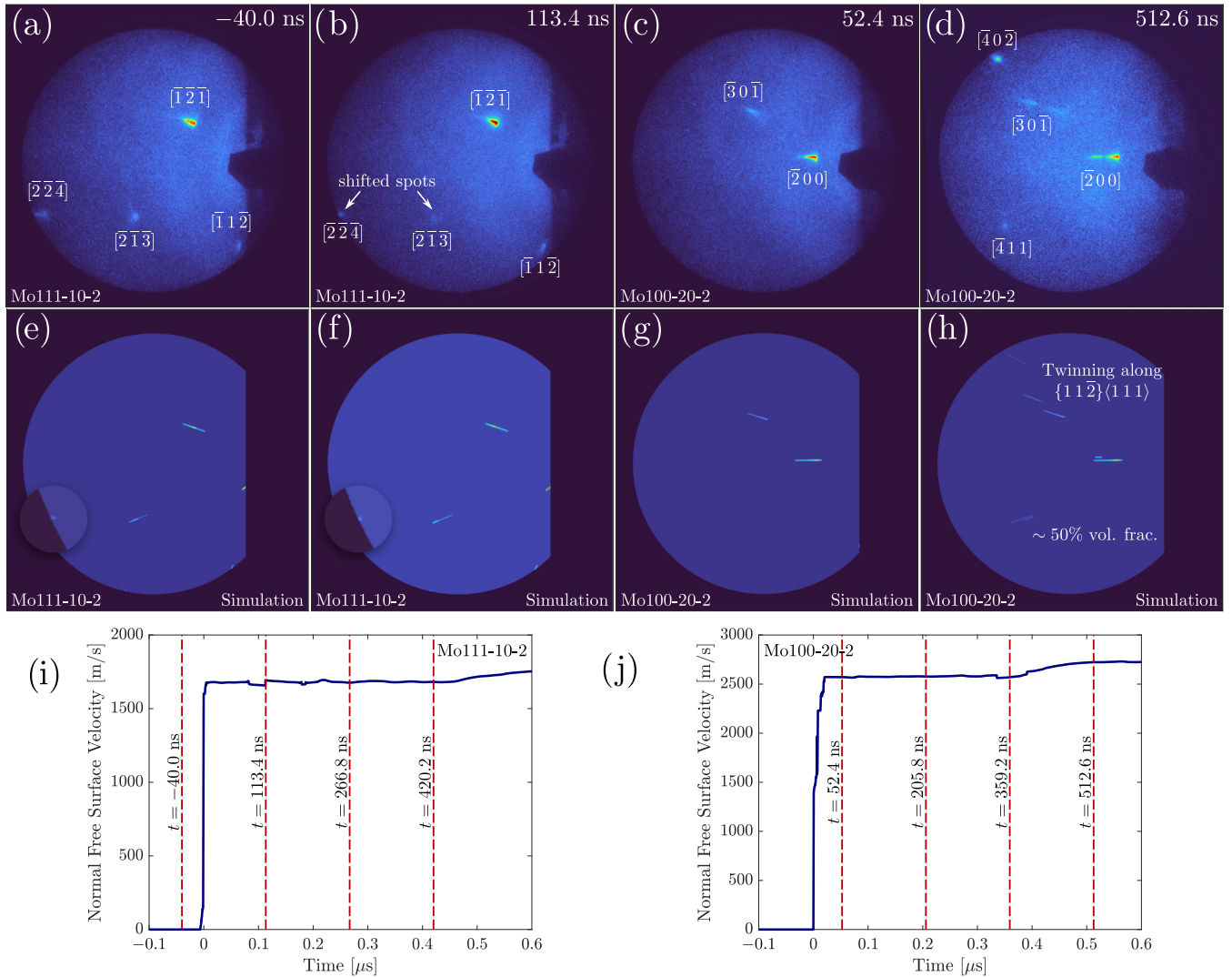


FIG. 2. (a)–(d) Experimentally obtained XRD frames which show both spots shifting due to compression and deformation twinning at higher pressure during the unloading. The diffraction spots are labeled using (e)–(h) for the respective XRD simulations incorporating both compression and twinning behavior. (i)–(j) The interferometry data are also shown indicating the time instances of XRD frame captures.

the sample is rotated in simulation along its outward normal and the procedure is repeated until the diffraction spots match experimental results.

Once these spots have been indexed, the lattice strains and stresses can be determined from the observed shifts in experimental diffraction spots. It can be shown that the ambient scattering vector  $\mathbf{g}_{hkl}$  in the reciprocal space is related to the scattering vector of the deformed lattices,  $\mathbf{g}_{hkl}^d$ , through the deformation gradient ( $\mathbf{F}$ ),  $\mathbf{g}_{hkl}^d = \mathbf{F}^{-T} \mathbf{g}_{hkl}$  [40]. However,

the deformation gradient has nine unknowns but each experiment does not contain enough information to resolve all nine components. Since each experiment typically contains two to four diffraction spots and plate impact experiments are conducted under uniaxial strain conditions, an infinitesimal strain ( $\epsilon$ ) linearization ( $\mathbf{F} = \mathbf{I} + \epsilon$ ) and plane strain assumption was employed to uniquely determine the elastic strain tensor. This was done through an optimization problem where the objective function was

$$\mathcal{O} = \min_{\mathbf{F}^{-T}} \left( \sum_{i=1}^M \sum_{n=1}^N \left\| \mathbf{F}^{-T} \Delta \mathbf{k}^n - \hat{\mathbf{k}}^n \right\| \left\| \mathbf{F}^{-T} \Delta \mathbf{k}^n + \mathbf{k}_0^n(\lambda_i^n) \right\| + \mathbf{k}_0^n(\lambda_i^n) \right). \quad (1)$$

Here, the incident vector  $\mathbf{k}_0$  for a given wavelength  $\lambda_i$  is known. Additionally, the scattering vector,  $\Delta \mathbf{k} = \mathbf{g}_{hkl}$ , and the direction of the diffracted vectors  $\hat{\mathbf{k}}$  from back projecting each indexed diffraction spot to the sample location are known.

Thus, the goal is to determine the deformation gradient  $\mathbf{F}$  that minimizes the objective function from Eq. (1). Details of the XRD simulation methodology and validation can be found in Secs. III and IV of the SM, respectively.

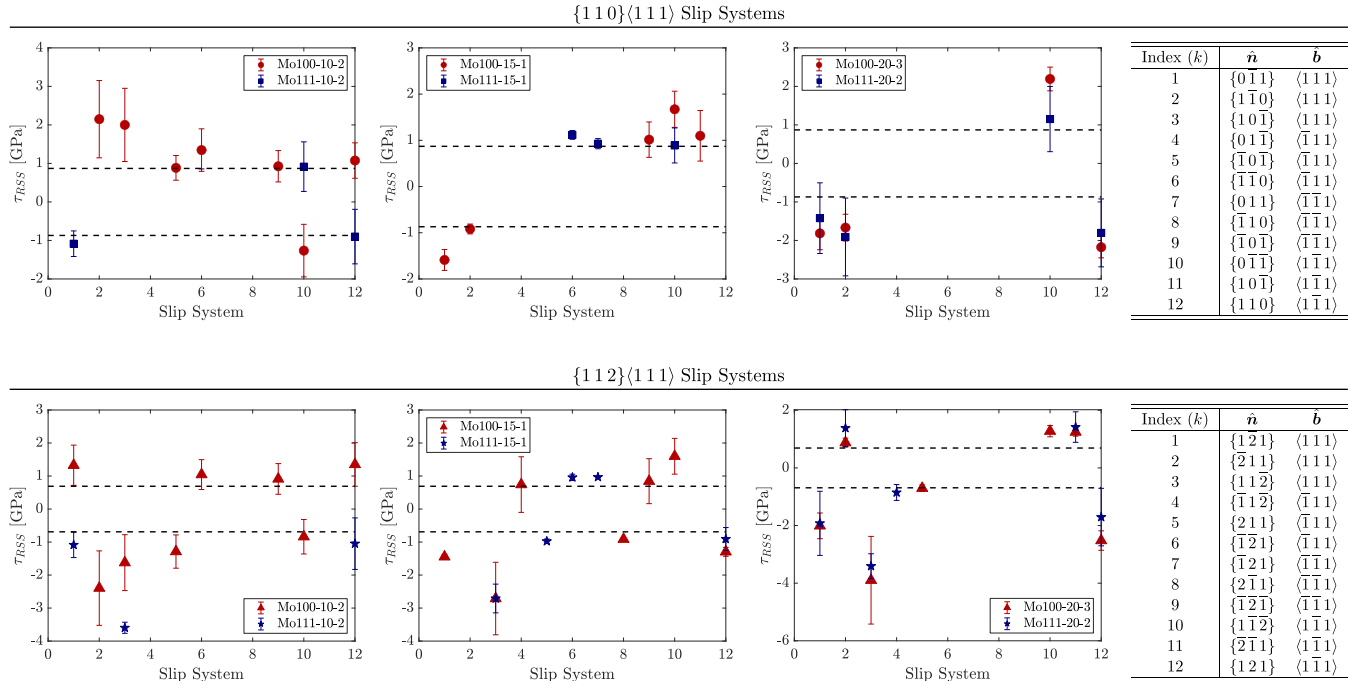


FIG. 3. Resolved shear stress ( $\tau_{\text{rss}}$ ) along the 12 different  $\{110\}\langle 111 \rangle$  and  $\{112\}\langle 111 \rangle$  slip systems of bcc single crystal for orientations  $[100]$  and  $[111]$  molybdenum crystals at pressures ranging from 10–20 GPa. Only the data above the critical resolved shear stresses (dashed lines) are shown.

#### IV. RESULTS

XRD simulations were conducted for all experiments from which we propose that the shock compression behavior of molybdenum single crystals is governed by dislocation slip regardless of crystal orientation and impact stress. To further investigate this observation, the resolved shear stresses along the  $\{110\}\langle 111 \rangle$  and  $\{112\}\langle 111 \rangle$  slip systems were calculated and plotted in Fig. 3. It is apparent that both these systems are active at the Hugoniot state for the two orientations where the  $\{110\}\langle 111 \rangle$  contributes to slip in the antitwinning sense and  $\{112\}\langle 111 \rangle$  in the twinning. Additionally, the resolved shear stress magnitudes are similar for both orientations with the  $\{11\bar{2}\}\langle 111 \rangle$  system being the most active. This explains the consistent peak Hugoniot velocity observed from the continuum measurements for both orientations for the same impact velocity and matches previous work by Oniyama *et al.* [33]. They reported that the shock velocity–particle velocity ( $U_s$ - $u_p$ ) equations of state for the different molybdenum crystal orientations were very similar to within experimental uncertainty, similarly to previous literature on fcc metals such as copper [41] and aluminum [42]. This implies that while single crystals exhibit orientation dependence at the elastic limit, no anisotropy may be present for the Hugoniot response of cubic crystals.

While the experiments in this study probed the diffraction spot evolution at the Hugoniot state, using the resolved stresses in Fig. 3, we anticipate the anisotropy at the elastic limit could stem from the larger number of slip systems activated for  $[100]$  orientation seen for the lowest stress experiment ( $\sim 9$  GPa) which are the closest to the elastic limit of the two orientations. An alternate possibility is related to the cubic symmetry of the stiffness tensor. For example, consider

a uniaxial elastic strain of 1% for both the  $[100]$  and  $[111]$  single crystals. The maximum and minimum principal stress for the  $[100]$  is 466 MPa and 163 MPa respectively whereas for  $[111]$  it is 410 MPa and 191 MPa. This clearly implies that the shear stresses along the  $[100]$  orientation will be larger due to the anisotropy in the stiffness tensor and thus justifies the observed lower elastic limit than for the  $[111]$  orientation. Using this argument, the previous anisotropy in the elastic limit is justified as the lattice strains obtained for these experiments on  $[100]$  and  $[111]$  molybdenum were comparable at similar pressures. Thus, larger shear strains were present for the  $[100]$  crystals than the  $[111]$  and this is illustrated in Fig. 3.

At the highest pressures ( $> 16$  GPa), during unloading, new diffraction spots were observed along with preexisting spots splitting up. An example of this is shown in Fig. 2(d). This indicates that deformation twinning, which has been previously observed for shock-compressed molybdenum [23,24], possibly governs the unloading behavior of Mo single crystals similar to what was observed for magnesium [43]. To determine the relevant twin systems, an additional contribution to the deformation gradient from twinning,  $F_t$ , was incorporated in the simulations such that  $F_t = I + \gamma \hat{b} \otimes \hat{n}$ . Here,  $I$  is the identity tensor,  $\gamma = \frac{1}{\sqrt{2}}$  is the twinning shear magnitude [44], and  $\hat{n}$  and  $\hat{b}$  are the twin plane normal and the twinning shear direction, respectively. The simulated diffraction with twinning is shown in Fig. 2(h). By iterating through all the possible  $\{112\}\langle 111 \rangle$  systems from Fig. 3, it was determined that twinning in both  $[100]$  and  $[111]$  molybdenum always occurred along the  $\{11\bar{2}\}\langle 111 \rangle$  system. This is consistent with the largest resolved shear stress observed along this system for all crystal orientations (Fig. 3).

Before discussing the possible mechanisms contributing to deformation twinning, it is important to note that the intensities of these new spots are weak but still easily discernible from ambient noise. This is expected because a partial constructive interference could still occur if atomic locations deviate slightly from their exact crystal structure, which satisfies the Laue condition. Furthermore, due to the abrupt nature of a shock wave and the isentropic release, the atomic arrangement undergoes a possible rearrangement across coherently diffracting domains. This affects the observed diffraction intensities and results in a mosaic spread that matches the smearing of the diffraction spots observed in the experiments. These weak intensity diffraction spots were also present in the work by Turneaure *et al.* [43], who also observed deformation twinning upon release in hexagonal close-packed magnesium. Additionally, while twinning is rather complex and results in multiple twin systems being activated, it is possible that these multiple systems are present in our experiments but at a very low volume fraction such that they get masked by ambient noise and cannot be distinguished. Nonetheless, the data provide strong evidence regarding possible twinning occurring during the release.

Multiple factors contribute to the nucleation and propagation of deformation twinning in bcc crystals such as pressure, strain rate, pre-straining, and grain size. Here, the Mo are single crystals and hence the grain size  $d$  can be assumed to be infinite. Thus, by the Hall-Petch scaling relation  $d^{-1/2}$  [14,44,45], larger grain sizes correspond to lower twinning shear stress. It was previously determined, using DFT calculations [46,47], that a shear stress of 1.4 GPa is sufficient to nucleate twins. While the magnitude of resolved shear stress along the  $\{1\ 1\ \bar{2}\}\langle 1\ 1\ 1\rangle$  system is beyond this critical value during compression, here, twinning only occurs during shock release. During unloading, the macroscopic normal stress decreases faster than the lateral stresses which results in a reverse yielding. Additionally, during release, the shear stress along the  $\{1\ 1\ \bar{2}\}\langle 1\ 1\ 1\rangle$  system reverses in direction. Since twinning is polarized [44] unlike slip, the reversal in direction due to unloading is critical to induce the nucleation of twins.

The passage of the compressive shock wave contributes to pre-straining and produces homogeneous nucleation of dislocations [44,45]. Earlier work on shock-compressed molybdenum and postmortem TEM analysis by Mahajan *et al.* [23] demonstrated that homogeneous dislocation field and pre-straining suppresses the formation of twins. However, during unloading, dislocation annihilation tends to occur [14,45] potentially generating a heterogeneous distribution similar to what Mahajan *et al.* [23] observed in their shock-recovered samples. With regard to pre-straining, Christian *et al.* [44] claim that the amount of pre-straining required to suppress twinning depends on the strain rate. Since the strain rates during release in our experiments are lower than during compression but still beyond  $10^5\ \text{s}^{-1}$ , this may be sufficient to

reduce the effect of pre-compression due to the shock wave. Additionally, based on the experiments conducted here, both shock and release behaviors of molybdenum at lower pressure are primarily governed by dislocation slip; however, the critical pressure describing the slip-to-twin transition [45] occurs around 16 GPa. This is much lower than the transition pressure for  $[0\ 0\ 1]$  copper [45] possibly due to the higher stacking fault energies in fcc metals. On the contrary, previous work by Wongwiwat *et al.* [24] and Mahajan *et al.* [23] observed twinning at lower pressures for polycrystalline Mo based on recovered samples possibly due to higher deviatoric stresses from grain-boundary interactions. This is consistent with what is observed for iron single crystals where the critical stress to induce phase transformation was lower for polycrystalline iron due to generally higher deviatoric stresses present than  $[1\ 0\ 0]$  iron [48].

## V. CONCLUSION

In summary, plate impact experiments with real-time x-ray diffraction were conducted to characterize the deformation mechanisms governing the elastic-plastic compression of molybdenum single crystals. We observe that the shock compression and release behavior is dominated by dislocation slip along  $\{1\ 1\ 0\}\langle 1\ 1\ 1\rangle$  and  $\{1\ 1\ \bar{2}\}\langle 1\ 1\ 1\rangle$  slip systems for both  $[1\ 0\ 0]$  and  $[1\ 1\ 1]$  crystal orientations. However, at normal stresses beyond 16 GPa,  $\{1\ 1\ \bar{2}\}\langle 1\ 1\ 1\rangle$  twins are nucleated during unloading. This explains why the loading orientation does not effect the Hugoniot response and the anisotropy only affects the elastic-plastic transition. Future works will aim to explore the shock-and-release behaviors at higher stress, at varying strain rates, and at varying pulse duration to better characterize the mechanisms contributing to the onset of twinning and understand its role on material strength. Additionally, exploring the role of grain boundaries on the elastic-to-plastic transition and the shock-release behavior would be an interesting next step.

## ACKNOWLEDGMENTS

The authors gratefully acknowledge the support of DOE/NNSA Award No. DE-NA0003957. The authors also thank Zev Lovinger, James Hawreliak, Paulo Rigg, Stefan Turneaure, Pritha Reganathan, Adam Schumann, and the DCS staff for their help with designing, conducting, and processing the experiments. This publication is based on work performed at the Dynamic Compression Sector, which is operated by Washington State University under the U.S. Department of Energy (DOE)/National Nuclear Security Administration Award No. DE-NA0003957. This research used resources of the Advanced Photon Source, a DOE Office of Science User Facility operated for the DOE Office of Science by Argonne National Laboratory under Contract No. DE-AC02-06CH11357.

[1] M. A. Meyers, *Dynamic Behavior of Materials* (John Wiley & Sons, New York, NY, 1994).

[2] R. F. Smith, D. E. Fratanduono, D. G. Braun, T. S. Duffy, J. K. Wicks, P. M. Celliers, S. J. Ali, A. Fernandez-Pañella,

- R. G. Kraus, D. C. Swift *et al.*, *Nat. Astronomy* **2**, 452 (2018).
- [3] M. Itoh, M. Katayama, and R. Rainsberger, *Mater. Sci. Forum* **465-466**, 73 (2004).
- [4] G. A. Graham, A. T. Kearsley, I. P. Wright, M. J. Burchell, and E. A. Taylor, *Int. J. Impact Eng.* **29**, 307 (2003).
- [5] D. Sandstrom, *Los Alamos Science* **17**, 36 (1989).
- [6] Y. M. Gupta, S. J. Turneaure, K. Perkins, K. Zimmerman, N. Arganbright, G. Shen, and P. Chow, *Rev. Sci. Instrum.* **83**, 123905 (2012).
- [7] J. A. Hawreliak and S. J. Turneaure, *J. Appl. Phys.* **129**, 135901 (2021).
- [8] S. J. Tracy, S. J. Turneaure, and T. S. Duffy, *Phys. Rev. Lett.* **120**, 135702 (2018).
- [9] S. J. Turneaure, S. M. Sharma, and Y. M. Gupta, *Phys. Rev. Lett.* **125**, 215702 (2020).
- [10] P. Renganathan, S. J. Turneaure, S. M. Sharma, and Y. M. Gupta, *Phys. Rev. B* **99**, 134101 (2019).
- [11] S. J. Turneaure, S. M. Sharma, and Y. M. Gupta, *Phys. Rev. Lett.* **121**, 135701 (2018).
- [12] J. Wadsworth, T. G. Nieh, and J. J. Stephens, *Int. Mater. Rev.* **33**, 131 (1988).
- [13] C. R. Weinberger, B. L. Boyce, and C. C. Battaile, *Int. Mater. Rev.* **58**, 296 (2013).
- [14] M. Sliwa, D. McGonegle, C. Wehrenberg, C. A. Bolme, P. G. Heighway, A. Higginbotham, A. Lazicki, H. J. Lee, B. Nagler, H. S. Park, R. E. Rudd, M. J. Suggit, D. Swift, F. Tavella, L. Zepeda-Ruiz, B. A. Remington, and J. S. Wark, *Phys. Rev. Lett.* **120**, 265502 (2018).
- [15] L. Hollang, D. Brunner, and A. Seeger, *Mater. Sci. Eng. A* **319-321**, 233 (2001).
- [16] S. S. Lau and J. E. Dorn, *Phys. Status Solidi A* **2**, 825 (1970).
- [17] S. Lau, S. Ranji, A. Mukherjee, G. Thomas, and J. Dorn, *Acta Metall.* **15**, 237 (1967).
- [18] J. Y. Kim and J. R. Greer, *Acta Mater.* **57**, 5245 (2009).
- [19] A. Seeger, *J. Phys. IV* **05**, C7-45 (1995).
- [20] A. Seeger, *Mater. Sci. Eng. A* **319-321**, 254 (2001).
- [21] G. J. Irwin, F. Guiu, and P. L. Pratt, *Phys. Status Solidi A* **22**, 685 (1974).
- [22] A. Seeger and L. Hollang, *Mater. Trans. JIM* **41**, 141 (2000).
- [23] S. Mahajan and A. Bartlett, *Acta Metall.* **19**, 1111 (1971).
- [24] K. Wongwivat and L. Murr, *Mater. Sci. Eng.* **35**, 273 (1978).
- [25] D. Santamaría-Pérez, M. Ross, D. Errandonea, G. D. Mukherjee, M. Mezouar, and R. Boehler, *J. Chem. Phys.* **130**, 124509 (2009).
- [26] R. S. Hixson and J. N. Fritz, *J. Appl. Phys.* **71**, 1721 (1992).
- [27] J. H. Nguyen, M. C. Akin, R. Chau, D. E. Fratanduono, W. P. Ambrose, O. V. Fatyanov, P. D. Asimow, and N. C. Holmes, *Phys. Rev. B* **89**, 174109 (2014).
- [28] J. Wang, F. Coppari, R. F. Smith, J. H. Eggert, A. E. Lazicki, D. E. Fratanduono, J. R. Rygg, T. R. Boehly, G. W. Collins, and T. S. Duffy, *Phys. Rev. B* **94**, 104102 (2016).
- [29] G. I. Kanel, S. V. Razorenov, A. V. Utkin, V. E. Fortov, K. Baumung, H. U. Karow, D. Rusch, and V. Licht, *J. Appl. Phys.* **74**, 7162 (1993).
- [30] A. Mandal and Y. M. Gupta, *J. Appl. Phys.* **121**, 045903 (2017).
- [31] A. Mandal and Y. M. Gupta, *J. Appl. Phys.* **125**, 055903 (2019).
- [32] T. Oniyama, Y. M. Gupta, and G. Ravichandran, *J. Appl. Phys.* **127**, 205902 (2020).
- [33] T. Oniyama, Y. M. Gupta, and G. Ravichandran, *J. Appl. Phys.* **129**, 245906 (2021).
- [34] See Supplemental Material at <http://link.aps.org/supplemental/10.1103/PhysRevMaterials.7.073601> for additional details regarding the experimental results (real-time XRD and velocity interferometry results), and additional details on XRD modeling, which includes Ref. [49].
- [35] S. J. Turneaure, N. Sinclair, and Y. M. Gupta, *Phys. Rev. Lett.* **117**, 045502 (2016).
- [36] T. J. Volz, Ph.D. thesis, Washington State University, 2020, <https://hdl.handle.net/2376/111551>.
- [37] The MathWorks Inc., MATLAB version 9.13.0 (R2021b) (The Mathworks, Inc., Natick, Massachusetts, 2021), <https://www.mathworks.com>.
- [38] C. Prescher and V. B. Prakapenka, *High Press. Res.* **35**, 223 (2015).
- [39] O. T. Strand, D. Goosman, C. Martinez, T. Whitworth, and W. Kuhlow, *Rev. Sci. Instrum.* **77**, 083108 (2006).
- [40] M. Miller, Polycrystalline Diffraction—A Primer for the 2016 APS NX School (Oak Ridge National Laboratory, 2017).
- [41] R. Chau, J. Stölken, P. Asoka-Kumar, M. Kumar, and N. C. Holmes, *J. Appl. Phys.* **107**, 023506 (2010).
- [42] D. Choudhuri and Y. M. Gupta, *J. Appl. Phys.* **114**, 153504 (2013).
- [43] S. J. Turneaure, P. Renganathan, J. M. Winey, and Y. M. Gupta, *Phys. Rev. Lett.* **120**, 265503 (2018).
- [44] J. Christian and S. Mahajan, *Prog. Mater. Sci.* **39**, 1 (1995).
- [45] M. Meyers, H. Jarmakani, E. Bringa, and B. Remington, in *Dislocations in Solids*, edited by J. Hirth and L. Kubin (North-Holland, Boston, MA, 2009), Vol. 15, pp. 91–197.
- [46] S. Ogata, J. Li, and S. Yip, *Europhys. Lett.* **68**, 405 (2004).
- [47] S. Ogata, J. Li, and S. Yip, *Phys. Rev. B* **71**, 224102 (2005).
- [48] B. J. Jensen, G. T. Gray, and R. S. Hixson, *J. Appl. Phys.* **105**, 103502 (2009).
- [49] B. Fultz and J. Howe, *Transmission Electron Microscopy and Diffractometry of Materials* (Springer Science & Business Media, New York, NY, 2013).